



doi:10.1016/j.gca.2004.07.028

## Weathering geochronology by (U-Th)/He dating of goethite

DAVID L. SHUSTER,<sup>1,\*</sup> PAULO M. VASCONCELOS,<sup>2</sup> JONATHAN A. HEIM<sup>2</sup> and KENNETH A. FARLEY<sup>1</sup><sup>1</sup>Division of Geological and Planetary Sciences, MC 100-23, California Institute of Technology, Pasadena, CA 91125, USA<sup>2</sup>Department of Earth Sciences, University of Queensland, Brisbane, Queensland 4072, Australia

(Received March 19, 2004; accepted in revised form July 30, 2004)

**Abstract**—Nine samples of supergene goethite (FeOOH) from Brazil and Australia were selected to test the suitability of this mineral for (U-Th)/He dating. Measured He ages ranged from 61 to 8 Ma and were reproducible to better than a few percent despite very large variations in [U] and [Th]. In all samples with internal stratigraphy or independent age constraints, the He ages corroborated the expected relationships. These data demonstrate that internally consistent He ages can be obtained on goethite, but do not prove quantitative <sup>4</sup>He retention. To assess possible diffusive He loss, stepped-heating experiments were performed on two goethite samples that were subjected to proton irradiation to produce a homogeneous distribution of spallogenic <sup>3</sup>He. The <sup>3</sup>He release pattern indicates the presence of at least two diffusion domains, one with high helium retentivity and the other with very low retentivity at Earth surface conditions. The low retentivity domain, which accounts for ~ 5% of <sup>3</sup>He, contains no natural <sup>4</sup>He and may represent poorly crystalline or intergranular material which has lost all radiogenic <sup>4</sup>He by diffusion in nature. Diffusive loss of <sup>3</sup>He from the high retentivity domain is independent of the macroscopic dimensions of the analyzed polycrystalline aggregate, so probably represents diffusion from individual micrometer-size goethite crystals. The <sup>4</sup>He/<sup>3</sup>He evolution during the incremental heating experiments shows that the high retentivity domain has retained 90%–95% of its radiogenic helium. This degree of retentivity is in excellent agreement with that independently predicted from the helium diffusion coefficients extrapolated to Earth surface temperature and held for the appropriate duration. Considering both the high and low retentivity domains, these data indicate that one of the samples retained 90% of its radiogenic <sup>4</sup>He over 47.5 Ma and the other retained 86% over 12.3 Ma. Thus while diffusive-loss corrections to supergene goethite He ages are required, these initial results indicate that the corrections are not extremely large and can be rigorously quantified using the proton-irradiation <sup>4</sup>He/<sup>3</sup>He method. Copyright © 2005 Elsevier Ltd

### 1. INTRODUCTION

Weathering profiles provide a record of chemical and physical processes occurring at the surface of terrestrial planets. Their mineralogical and geochemical compositions record information on the composition and abundance of weathering solutions, and their depth and complexity provide insight to the longevity of their development and the role that climate and biologic processes have in enhancing weathering processes. The global distribution of weathering profiles reflects rainfall and temperature gradients across the planet. The profiles also reflect the balance between chemical-physical weathering and chemical-physical erosion, providing insight into landscape evolution and global geochemical cycles.

The thermodynamic stability and slow dissolution kinetics of many supergene minerals found in weathering profiles favors their preservation under earth surface conditions, making them useful recorders of paleoenvironmental conditions. Because deeply weathered profiles occur on most continents and appear to have formed over a wide range of geologic times, they potentially represent a powerful record of continental paleoenvironments. Savin and Epstein (1970) first proposed the combined use of O and H isotope systematics in weathering minerals to reconstruct continental paleoclimates. Experimentally determined O and H isotopic fractionation factors have been widely applied to quantify paleotemperatures during goethite

and kaolinite precipitation (Yapp, 1987; Yapp, 1990; Bird and Chivas, 1993; Lawrence and Meaux, 1993; Girard et al., 1997; Giral-Kacmarcik et al., 1998; Girard et al., 2000; Yapp, 2000). Yapp (2000) demonstrated that supergene goethite (FeOOH) can behave as a closed system with respect to O and H exchange for at least ~50 Myr. Despite the wealth of information recorded in weathering profiles, their usefulness as paleoclimatic and paleoenvironmental indicators is limited by the paucity of information on their timing and rate of formation.

An understanding of weathering profile evolution and derivation of paleoclimatic information from these potential archives requires quantitative knowledge of the timing of specific weathering reactions and measurements of the rate of propagation of weathering fronts. Advances have recently been made in these areas (Vasconcelos et al., 1992; Brown et al., 1994; Vasconcelos et al., 1994b; Dequincey et al., 1999). In young weathering profiles (< 1Ma), weathering geochronology by U-Th decay series dating of pedogenic carbonate and silica minerals provides reliable information on timing of mineral precipitation (Sharp et al., 2003). In older weathering profiles hosting supergene K-bearing minerals, weathering geochronology by the K-Ar and <sup>40</sup>Ar/<sup>39</sup>Ar methods are useful. Vasconcelos et al. (1994a, 1994b); Dammer et al. (1996, 1999); Ruffet et al. (1996); Hénocque et al. (1998); Hautmann and Lippolt (2000) applied <sup>40</sup>Ar/<sup>39</sup>Ar dating to K bearing Mn-oxides (cryptomelane) and sulphates (alunite-jarosite) from profiles in South America, Africa, Australia, and Europe. Precipitation ages ranging from ~70 Ma to modern suggest that some continental weathering profiles have been continuously ex-

\* Author to whom correspondence should be addressed (dshuster@caltech.edu).

posed at least since the Cretaceous. Dequincey et al. (2002) measured major and trace element abundances and  $^{238}\text{U}$ - $^{234}\text{U}$ - $^{230}\text{Th}$  activity ratios in bulk rock samples from a 15m-thick African lateritic profile. They found evidence of recent U mobility throughout the laterite, possibly initiated by a late Pleistocene climatic shift, and suggested two episodes of laterite formation. In situ produced cosmogenic nuclides have also been used to constrain the mechanisms of weathering profile development (Brown et al., 1994; Braucher et al., 1998; Braucher et al., 2000). Braucher et al. (2000) interpreted homogeneous  $^{10}\text{Be}$  and  $^{26}\text{Al}$  concentrations in quartz in the uppermost  $\sim 2\text{m}$  and an exponential decrease in the lower  $\sim 8\text{m}$  of a 10 m lateritic soil profile to indicate bioturbation of the surface layer. Small et al. (1999) and Riebe et al. (2003) used the accumulation of  $^{10}\text{Be}$  and  $^{26}\text{Al}$ , combined with mass balance calculations, to infer rates of regolith production.

Lateritic weathering profiles, often more than 400 m thick, host a plethora of supergene iron minerals distributed from the surface (in loose pisoliths and ferruginous duricrusts), through the mottled zone, and down into the saprolite and the weathering-bedrock interface. These lateritic profiles are texturally and geochemically complex and it is difficult to distinguish between relict features and those resulting from ongoing processes. A variety of geochemical and petrological tools have been employed to characterize the superimposed horizons (ferricrete, mottled zone, saprolite, etc.) common to complete lateritic weathering profiles (e.g., Anand and Paine, 2002). In detail, these studies reveal that lateritic profiles represent the result of successive and ongoing geochemical, geomorphological and biologic processes. The great depth and complexity of lateritic weathering profiles, combined with the abundance of supergene iron minerals throughout the profile, suggest that the development of a methodology suitable for dating supergene iron oxides and hydroxides may significantly improve our understanding of the paleoclimatic and environmental conditions controlling continental weathering.

Because weathering products usually precipitate and reside at near surface temperatures, and because such conditions are favorable for slow helium diffusion, we have investigated whether radiogenic helium is quantitatively retained in supergene goethite. If  $^4\text{He}$ , U and Th are immobile in a mineral produced via weathering, the (U-Th)/He age represents the time since its precipitation. Due to its rapid radiogenic evolution, the (U-Th)/He system offers potential to date, to high resolution, a variety of supergene minerals that contain even trace amounts of U and/or Th over a range of timescales ( $\sim 0.5\text{ Ma}$  to  $\sim 100\text{ Ma}$ ).

The application of (U-Th)/He dating to Fe-oxides is not a new idea, but has recently come under renewed study. Strutt (1910) reported the first He age measured on a limonite ( $\sim 2\text{Fe}_2\text{O}_3 \cdot 3\text{H}_2\text{O}$ ;  $\sim 140\text{ Ma}$ ). More recently, Lippolt and others reported a dozen He ages on hydrothermal and supergene goethites (FeOOH), limonites (Lippolt et al., 1998) and hydrothermal hematites ( $\text{Fe}_2\text{O}_3$ ) (Wernicke and Lippolt, 1993; Baehr et al., 1994; Wernicke and Lippolt, 1994a; Wernicke and Lippolt, 1994b; Lippolt et al., 1995) from central Europe. The reported hematite He ages are as young as  $\sim 5\text{ Ma}$  and as old as  $\sim 180\text{ Ma}$ . Helium-4 diffusion experiments (Baehr et al., 1994; Wernicke and Lippolt, 1994a), comparisons with coexisting adularia and biotite K/Ar ages and tests for internal consistency

(Lippolt et al., 1995) all indicate that geologically significant He ages can be determined on certain samples of hydrothermal hematite. The goethite He ages determined by Lippolt et al. (1998) span from  $\sim 0.8\text{ Ma}$  to  $\sim 130\text{ Ma}$ , qualitatively indicating helium retention over geologic timescales. They concluded that (U-Th)/He dating of goethite is potentially useful for dating very young crustal movements. However, a quantitative description of helium diffusivity in these materials at Earth surface conditions is required to establish the significance of these ages.

In this work, we evaluated the helium retentivity of polycrystalline aggregates of supergene goethite (FeOOH). We chose goethite due to its ubiquity, because it often contains high uranium concentrations in the weathering environment (Giammer, 2001), and because U in goethite may occupy well defined crystallographic sites (Duff et al., 2002). Our approach was both empiric and experimental. The empiric approach tested He age reproducibility and U and Th concentration homogeneity on multiple aliquots of individual samples. We also compared Fe-oxide He ages with cryptomelane  $^{40}\text{Ar}/^{39}\text{Ar}$  ages from the same weathering profiles, one directly associated goethite/cryptomelane pair, and of regionally associated samples. The experimental approach involved vacuum diffusion experiments on proton-irradiated polycrystalline goethite to determine the temperature dependence of helium diffusivity, from which we were able to characterize  $^4\text{He}$  retentivity at Earth surface temperatures. We conducted stepwise degassing experiments in which we measured both the natural radiogenic  $^4\text{He}$  and the spallogenic  $^3\text{He}$  induced by proton bombardment (Shuster and Farley, 2004; Shuster et al., 2004).

## 2. SAMPLES

For this study, we selected goethite based on several criteria: (1) in most cases, they were precipitated directly from weathering solutions into cavities created by the dissolution of primary sulfides or carbonates; (2) they exhibited botryoidal growth habits recording relative timing of mineral precipitation; (3) they were pure and devoid of primary contaminants; (4) they were composed of aggregated goethite crystallites ( $< 1\ \mu\text{m}$ ); (5) they were associated with other datable supergene phases (i.e., cryptomelane), and their relative timing of precipitation could be determined based on textural relationships. Efforts were taken to ensure that aliquots of each sample were from a single generation of goethite. Two samples were then selected for detailed stepwise degassing diffusion experiments. We briefly describe the nine goethite samples below.

The four Bahia goethites (BAH-F124-111.2, 114, 118, and 123) are vitreous, botryoidal, of high purity, and precipitated from solution into empty cavities, which based on their morphology are known to have created during the dissolution of primary pyrite, chalcopyrite, and calcite (Fig. 1). Because these samples precipitated from solution, they are unlikely to have contained detrital grains of un-weathered  $^4\text{He}$  bearing phases. The four samples were collected from a drill core from the weathering profile associated with the Igarapé Bahia Cu-Au deposit, Carajás, Brazil, from a drill-hole depth of  $\sim 110$ – $120\text{ m}$ , equivalent to a vertical depth of ca. 80m below the present surface; they precipitated and subsequently resided at depth throughout their existence. Multiple aliquots of samples 111.2

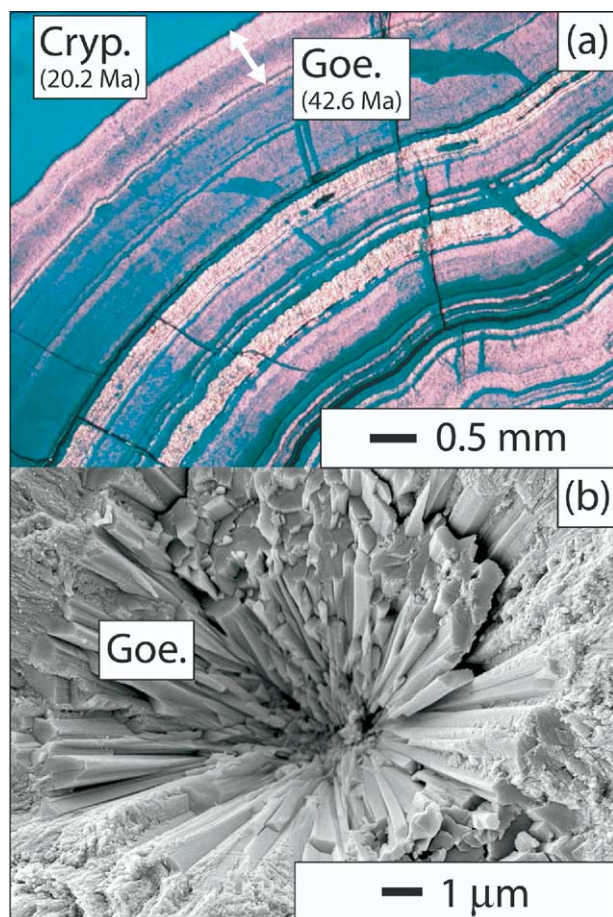


Fig. 1. Microscopy. (a). Combined reflected and transmitted light image of alternating bands of botryoidal goethite (dark red, translucent) and cryptomelane (gray, opaque) for sample BAH-F124-111.2. Each band records a distinct period of mineral precipitation from solution. Dating each band separately provides a stratigraphic test for the reliability of the (U-Th)/He ages obtained. Also shown is the raw He age (42.6 Ma) of the goethite growth band approximately indicated by the white arrow, and the  $^{40}\text{Ar}/^{39}\text{Ar}$  age (20.2 Ma) of the directly adjacent massive cryptomelane overgrowth. (b) Scanning electron microscopy (SEM) image of radial goethite crystals of sample BAH-F124-114 precipitated into empty cavities in the Igarapé Bahia weathering profile. The bladed goethite crystals with minimum dimension  $\sim 0.5 \mu\text{m}$  probably represent the high retentivity sites while the intergranular space represents the low retentivity sites. The finely crystalline material along the borders represents nucleation sites for a new generation of bladed crystals.

and 114 were prepared for He age reproducibility tests. Small pieces of the goethite bands were broken off, and then further divided into aliquots for multiple analyses. For instance BAH-F124-114-(a) is a  $\sim 10 \text{ mg}$  piece of the BAH-F124-114 goethite growth band and BAH-F124-114-(a)-1 is one of the 9 subaliquots prepared for analysis from that piece. Likewise BAH-F124-114-(b) is another piece sampled from the same growth band. We expect that each aliquot has approximately the same precipitation age. Figure 1b shows that the crystallites are  $\sim 0.5 \mu\text{m}$  in their minimum dimension.

The MI-2000-09 sample comes from a gossan at the Lake Moondarra Cu-prospect in the Mount Isa region, NE Australia. The sample is also associated with cavities formed in a quartz

veins by the dissolution of primary sulfides and carbonates during weathering reactions. These cavities often contain iron and manganese oxides and hydroxides. Several cryptomelane samples from a nearby outcrop and another outcrop in the same area, have been previously dated by the  $^{40}\text{Ar}/^{39}\text{Ar}$  method (Vasconcelos, 1998).

Sample B01-009 is a 15 cm hand specimen from the N4E iron mine in Carajás, Brazil. The sample is from the surface “canga,” or lateritic iron ore associated with weathering of the Carajás banded iron formation. We analyzed four subsamples of B01-009 (labeled a,c,e,g) that were texturally identified as four distinct generations of goethite present in the sample. Paragenetic relationships expressed in the hand sample suggest precipitation ages decrease in the order a,c,e,g.

### 3. METHODS

#### 3.1. He Dating

Using isotope-dilution mass spectrometry, we measured both [ $^4\text{He}$ ] (quadrupole), and [ $^{238}\text{U}$ ] and [ $^{232}\text{Th}$ ] (double-focusing ICP-MS) of individual sample aliquots. We extracted  $^4\text{He}$  from relatively larger aliquots ( $\sim 200 \mu\text{g}$ ) using a resistance furnace, and from smaller aliquots ( $\sim 5 \mu\text{g}$ ) using laser extraction. Details of the analytical techniques used for this study are described in Farley (2002) but modified as follows.

Because the individual goethite crystals are extremely small ( $\sim 1 \mu\text{m}$ ), the analyzed chips represent aggregates of  $\sim 10^7$  individual crystals. To eliminate the effects of  $\alpha$  ejection (Farley et al., 1996), we selected interior aliquots from mm-size botryoidal clusters. We verified mineral identification and ensured sample purity using Raman spectroscopy and powder X-ray diffractometry (XRD). The analyzed samples were greater than 99% FeOOH. Before analysis, we rinsed the aliquots in alcohol using sonication to remove small particulates adhered to the sample surfaces. To ensure quantitative transfer for U and Th analysis, we encapsulated the aliquots in Pt foil packets and used furnace and laser extraction temperatures of  $\sim 1150^\circ\text{C}$ . Following He extraction, we dissolved the Fe oxides in  $200 \mu\text{L}$  of concentrated HCl and heated for 12 hours to  $90^\circ\text{C}$ .  $^{230}\text{Th}$  and  $^{235}\text{U}$  spikes were added during dissolution.

For the He age calculations, we assumed (1) secular equilibrium among daughter nuclides in the  $^{238}\text{U}$  series; (2) a closed system for parents and daughters; and (3) zero initial  $^4\text{He}$  at the time of precipitation; these assumptions will be discussed below. Aliquots for furnace extraction were weighed before analysis to permit calculation of parent and daughter concentrations. For laser extraction, the masses of the Fe oxides were estimated by measuring the Fe concentration in solution. Because these masses are fairly uncertain, the concentrations are only approximate; however note that calculated He ages are independent of mass.

#### 3.2. Step-Heating Diffusion Experiments

Details of the stepwise degassing method used in this study were described by Shuster et al. (2004). The samples were held at a known temperature ( $T$ ) for a known amount of time ( $t$ ) in a volume of  $\sim 300 \text{ cm}^3$  under static vacuum. Following a heating step, the accumulated  $^3\text{He}$  and  $^4\text{He}$  were measured by sector field mass spectrometry using external standard calibration.

We converted measured helium release-fractions to diffusion coefficients ( $D/a^2$  where  $a$  is the diffusion domain radius) for each temperature step assuming spherical geometry (Fechtig and Kalbitzer, 1966). The calculation assumes an initially uniform spatial distribution of the diffusant. This assumption may not be valid if diffusion has affected the radiogenic  $^4\text{He}$  distribution; a diffusively modified  $^4\text{He}$  distribution will yield underestimates of  $D/a^2$  by this method.

To test for potential  $^4\text{He}$  losses, we bombarded our samples with  $\sim 10^{14}$  protons/ $\text{cm}^2$  using a  $\sim 150 \text{ MeV}$  proton beam at the Harvard Cyclotron Laboratory to generate a uniform distribution of spallogenic  $^3\text{He}$ . Shuster et al. (2004) showed that proton bombardment yields a spatially uniform  $^3\text{He}$  distribution across individual crystals as large as  $\sim 180 \mu\text{m}$ , and that, at least for apatite and titanite, the irradiation itself

Table 1. Replicate goethite He ages.

Sample	He Age (Ma)	(+/-)	[U] (ppm)	[Th] (ppm)	[ <sup>4</sup> He] (nmol/gm)	Sample	He Age (Ma)	(+/-)	[U] (ppm)	[Th] (ppm)	[ <sup>4</sup> He] (nmol/gm)
Furnace Extraction:						Furnace Extraction:					
BAH-F124-114-(a)-1	9.65	0.11	149.53	0.05	7.85	BAH-F124-111.2-(a)-1	n.d.	n.d.	55.84	0.04	n.d.
-(a)-2	10.03	0.11	152.79	0.03	8.33	-(a)-2	n.d.	n.d.	54.08	0.08	n.d.
-(a)-3	11.67	0.12	120.30	0.00	7.63	-(a)-3	n.d.	n.d.	49.54	0.14	n.d.
-(a)-4	10.08	0.11	156.17	0.00	8.56	-(a)-4	n.d.	n.d.	64.57	0.13	n.d.
-(a)-5	9.88	0.11	154.71	0.01	8.31	-(a)-5	n.d.	n.d.	64.31	0.88	n.d.
-(a)-6	10.14	0.11	162.31	<0.01	8.95	-(a)-6	41.71	0.47	28.24	0.14	6.44
-(a)-7	9.90	0.11	155.80	<0.01	8.39	-(a)-7	41.56	0.47	59.67	0.20	13.54
-(a)-8	10.78	0.12	15.79	<0.01	0.93	Mean/Std Err	41.64	0.08			
-(a)-9	10.34	0.12	160.46	<0.01	9.02						
Mean/Std Err	10.27	0.20									
Laser Extraction:						Laser Extraction:					
BAH-F124-114-(b)-1	10.18	0.11	325.63	0.03	18.02	BAH-F124-111.2-(b)-1	41.17	0.45	77.69	0.02	17.45
-(b)-2	10.70	0.12	368.81	0.05	21.47	-(b)-2	43.24	0.48	96.97	0.05	22.88
-(b)-3	10.95	0.12	329.83	0.02	19.64	-(b)-3	43.68	0.48	103.44	0.05	24.66
-(b)-4	11.36	0.12	288.13	0.01	17.80	-(b)-4	44.36	0.49	70.29	0.02	17.02
-(b)-5	11.86	0.13	250.95	0.02	16.18	Mean/Std Err	43.11	0.69			
Mean/Std Err	11.01	0.29				Grand Mean	42.62	0.53			
BAH-F124-114-(c)-1	10.63	0.15	312.68	0.03	18.08						
-(c)-2	10.81	0.12	265.29	0.06	15.60						
-(c)-3	11.74	0.15	246.92	<0.01	15.77						
-(c)-4	13.89	0.12	260.23	0.03	19.67						
-(c)-5	10.17	0.10	280.50	0.01	15.51						
-(c)-6	10.26	0.13	269.60	0.03	15.05						
-(c)-7	10.69	0.13	282.26	0.02	16.41						
-(c)-8	10.79	0.13	272.72	0.02	16.00						
-(c)-9	8.97	0.12	265.23	0.02	12.93						
Mean/Std Err	10.88	0.45									
Grand Mean	10.67	0.21									

The listed He age uncertainties are  $1\sigma$  propagated from U, Th and <sup>4</sup>He analytical uncertainties and underestimate true He age uncertainties. The U, Th and <sup>4</sup>He concentrations are approximations; calculated He ages are independent of mass. nmol is  $10^{-9}$  moles, “n.d.” denotes not determined.

does not change the <sup>4</sup>He diffusivity. In addition, because the proton-induced <sup>3</sup>He nuclei have approximately equal production probability from all target atoms present (Fe, Mn, O) with energies of ~1–10 MeV and because U-Th series  $\alpha$  particles have similar energies, we can assume that spallogenic <sup>3</sup>He and natural radiogenic <sup>4</sup>He atoms shared common stopping sites in diffusion domain(s) containing homogeneous U and Th (Shuster et al., 2004).

The advantages of proton-bombardment diffusion experiments for studying polycrystalline weathering products are that the helium (<sup>3</sup>He) distribution is uniform, and all diffusion domains contain <sup>3</sup>He at the start of stepwise degassing. Because we performed our diffusion experiments on polycrystalline aggregates, we expected a distribution of crystal sizes and potentially of diffusion domain sizes. In the same way that <sup>39</sup>Ar release fractions can be used to identify multiple diffusion domains in feldspar (Lovera et al., 1991), we used the <sup>3</sup>He release-fractions to constrain models which identify the presence and relative proportions of multiple diffusion domains within the samples and their function(s)  $D(T)/a^2$ . The proton bombardment technique allowed us to identify the release of <sup>3</sup>He from diffusion domains of sufficiently low retentivity to have lost most (or all) radiogenic <sup>4</sup>He over geologic time, but retentive enough to trap the spallogenic <sup>3</sup>He over weeks spent at room temperature between irradiation and analysis.

The stepped-heating experiments were performed on single-chip ~10 mg aliquots of Igarapé Bahia samples 114 and 111.2 (Fig. 1). These polycrystalline chips had radii of ~1 mm, though the individual goethite crystals are far smaller (~0.5  $\mu$ m). To investigate how chip size influences helium diffusivity, we performed a similar experiment on an aliquot of sample 114 with a radius of ~0.2 mm.

Because phase transitions of supergene Fe-oxides occur at low temperatures (Diakonov et al., 1994), the diffusion experiments were performed below ~250°C. Although we did not determine the sample mass before and after the actual diffusion experiments, we verified the stability of the samples by thermo-gravimetric analysis of separate aliquots under rough vacuum using the same thermal cycles as the diffusion experiments. An abrupt, ~10% decrease in mass was observed only at  $T > 250^\circ\text{C}$ , above the maximum temperatures of the diffusion experiments.

#### 4. HELIUM DATING—RESULTS

The measured [<sup>4</sup>He], [U], and [Th] and resulting goethite He ages are listed in Tables 1 and 2. Table 1 shows replicated analyses of samples 111.2 and 114, and Table 2 summarizes all of the goethite He ages and their comparator Ar ages. We measured <sup>3</sup>He/<sup>4</sup>He ratios on non-irradiated aliquots of these samples to be effectively zero ( $< 2.8 \times 10^{-8}$ ), indicating only radiogenic helium.

We observed a wide range in concentrations of [<sup>4</sup>He], [U], and [Th]; from ~0.04 to 23 nmol/g, 0.3 to 370 ppm, and <0.01 to 3.4 ppm, respectively. He ages range from ~61 to ~8 Ma. Th/U ratios are low (<0.1) for all goethite samples except those collected from the uppermost few meters of ferricrete from the N4E iron mine, Carajás, Brazil (B01-009 series), that have Th/U ranging from 2 to 10. The ranges in [U] and [Th] of eleven aliquots of sample 111.2 span factors of 4 and 44, respectively. We measured [<sup>4</sup>He] on six of these aliquots; the He ages differ by ~1.3% ( $42.6 \pm 0.5$  Ma;  $n = 6$ ). The [<sup>4</sup>He] and [U] of sample 114 span factors of 23 but the He ages vary by only 2% ( $10.7 \pm 0.2$  Ma;  $n = 23$ ). The He ages of the four B01-009 aliquots (a,c,e,g) also corroborate their paragenetic relations. As expected, the aliquot identified to be the youngest gave the youngest He age (8.3 Ma) and the oldest gave the oldest He age (61 Ma).

##### 4.1. Comparing He Ages with Ar Ages

The best way to test the accuracy of an absolute geochronometer is to compare it against an independently known mineral precipitation age. However, there are no other tech-

Table 2. Comparison between He and Ar ages, stratigraphic relationships.

Region:	phase	Sample	Radiometric age (Ma)	(+/-)	[U] (ppm)	[Th] (ppm)	[ <sup>4</sup> He] (nmol/gm)
Bahia:	goethites		(U-Th)/He				
		BAH-F124-111.2*	42.62	0.53	—	—	—
		BAH-F124-118	30.38	0.34	29.39	<0.01	4.87
		BAH-F124-123	15.80	0.18	29.00	<0.01	2.49
		BAH-F124-114*	10.67	0.21	—	—	—
		B01-009-(a) (oldest)	61.02	0.61	0.76	3.43	0.52
		B01-009-(c)	36.87	0.37	0.26	2.52	0.17
		B01-009-(e)	26.70	0.27	0.65	1.42	0.14
		B01-009-(g) (youngest)	8.33	0.08	0.36	2.00	0.04
		cryptomelanes		<sup>40</sup> Ar/ <sup>39</sup> Ar			
Regional range**	40 to 0		—	—	—	—	
		BAH-F124-111.2	20.2	0.56	—	—	—
Mount Isa:	goethite		(U-Th)/He				
		MI-2000-09	15.61	0.18	4.27	0.08	0.36
	cryptomelanes		<sup>40</sup> Ar/ <sup>39</sup> Ar				
Regional range		14.6 to 21.5	—	—	—	—	

Notes: The He age uncertainties are  $1\sigma$  propagated from U, Th and <sup>4</sup>He analytical uncertainties and underestimate true He age uncertainties. The U, Th and <sup>4</sup>He concentrations are approximations. Also reported are <sup>40</sup>Ar/<sup>39</sup>Ar ages determined on associated cryptomelane, where applicable. nmol is  $10^{-9}$  moles.

\* Average of replicate analyses (see Table 1).

\*\* Vasconcelos et al., 1994, “—” not applicable.

niques by which to directly date these minerals. An indirect comparison between different weathering phases is currently the only way to test the accuracy of the goethite (U-Th)/He ages.

The Bahia goethite He ages generally agree with cryptomelane <sup>40</sup>Ar/<sup>39</sup>Ar ages from the same profile, which range from ~40 to 0 Ma (Vasconcelos et al., 1994b). The eight goethite He ages in Table 2 fall in approximately this same range (~61 to 8 Ma). In the case of Bahia goethite sample 111.2 (He age ~43 Ma), two nearby samples (111.8 and 112.1) containing cryptomelane overgrowth on botryoidal goethite yield <sup>40</sup>Ar/<sup>39</sup>Ar ages of  $13.7 \pm 0.6$  and  $13.8 \pm 0.3$  Ma, consistent with the observed paragenetic relationship. Sample 111.2 contains a generation of cryptomelane that is directly precipitated over the goethite (Fig. 1). We do not necessarily expect that these two phases share a common precipitation age; however the cryptomelane age must be younger than the age of the goethite. The radiometric ages of the cryptomelane/goethite pair are consistent with their paragenetic relationship; the goethite He age is ~43 Ma whereas the three grains of cryptomelane from that sample yield <sup>40</sup>Ar/<sup>39</sup>Ar plateau ages of  $19.4 \pm 0.2$  Ma,  $20.6 \pm 0.2$ ,  $19.2 \pm 0.3$  and  $21.6 \pm 0.6$  Ma.

The He age for the Lake Moondarra sample MI-2000-09 (Table 2;  $15.61 \pm 0.18$  Ma) also agrees well with <sup>40</sup>Ar/<sup>39</sup>Ar ages from nearby samples (plateau ages of  $20.7 \pm 0.3$ ,  $19.7 \pm 0.1$ ,  $19.0 \pm 0.4$ ,  $16.0 \pm 1.7$ , and  $15.2 \pm 1.2$  Ma). The goethite and cryptomelane samples from the Lake Moondarra locality occur on a regionally recognized ca. 300 m-elevation weathering surface (Vasconcelos, 1998). The age of supergene minerals in some of these surfaces have been locally and regionally correlated (Vasconcelos and Conroy, 2003). Several other samples dated for the same surface in the Mt Isa Mines gossan, ~20 km away from the Lake Moondarra locality, yield cryptomelane <sup>40</sup>Ar/<sup>39</sup>Ar plateau ages of  $21.5 \pm 0.3$ ,  $21.2 \pm 0.5$ ,

$20.9 \pm 0.2$ ,  $20.7 \pm 0.2$ ,  $20.02 \pm 0.19$ ,  $18.0 \pm 0.3$ ,  $17.7 \pm 0.5$ ,  $16.7 \pm 0.2$ , and  $14.57 \pm 0.12$  Ma. The (U-Th)/He results obtained for the goethite sample is entirely consistent with the <sup>40</sup>Ar/<sup>39</sup>Ar plateau ages of cryptomelane ages from the same weathering profile. Goethite and Mn-oxides in the lake Moondarra site both reflect water-rock interaction during weathering of sulfide-carbonate hydrothermal assemblages. Once goethite and Mn-oxides precipitate, they will remain metastably preserved, particularly if after mineral precipitation the groundwater levels drop, leaving these minerals stranded in the unsaturated zone. A progressive drop of the water table is a predictable consequence of the known aridification of Australia since the Miocene.

## 5. HELIUM DATING—DISCUSSION

Three important results of the He dating study are that polycrystalline goethite contains (1) variable but generally ppm level concentrations of U and Th; (2) relatively high [<sup>4</sup>He]; and (3) He ages that are reproducible despite significant interaliquot variability in [U] and [Th]. The He age reproducibility, particularly despite strong [U] and [Th] variability, indicates systematic behavior in the polycrystalline goethite which precludes significant U and Th mobility (Farley et al., 2002). For example, uniform addition or removal of U from the goethite at some time following precipitation would not yield isochronous He ages in aliquots with variable U concentrations.

Each of the aliquots was originally located ~250  $\mu$ m from the next nearest aliquot and sampled from single massive generations of goethite. Since some samples have strongly heterogeneous U and Th concentrations between aliquots, commonality in their He ages requires that radiogenic <sup>4</sup>He atoms have not migrated between the aliquots (~125  $\mu$ m distance) since formation. Radiogenic helium was either quantitatively

retained or  $^4\text{He}$  diffusion resulted in loss of an identical fraction of  $^4\text{He}$  from each aliquot directly to the environment. Diffusive loss would require that  $^4\text{He}$  migrated along grain boundaries or another highly transmissive medium rather than through the crystals of the aggregate.

Corroboration of the paragenetic age relationship between the cryptomelane (younger) and goethite (older) by the He ages for sample 111.2 is also significant. Because diffusive helium loss and late stage U adsorption are processes likely to disrupt a goethite He age, and because both processes would result in an artificially young age, it is easier to reconcile systematically young He ages than old. Although the apparent  $\sim 20$  Myr hiatus between Fe-oxide and Mn-oxide precipitation is initially surprising, the precipitation timescales of coexisting phases are difficult to know a priori, particularly in the complicated processes of chemical weathering. The apparent  $\sim 20$  Myr hiatus between Fe-oxide and Mn-oxide precipitation is permissible, and may represent distinct weathering events in that region.

Once incorporated into goethite, the apparent immobility of U and Th implies that the goethite aggregates are resistant to post precipitation changes in groundwater chemistry. Dequincey et al. (2002) found evidence of recent U mobility throughout a lateritic profile in Africa by measuring U series activity ratios of homogenized whole rock samples. Their findings indicated that a recent (0.3 Ma) chemical remobilization had occurred throughout that system. They proposed that  $^{234}\text{U}$  could have been removed from the uppermost ferruginous unit (composed primarily of hematite and goethite) and redistributed throughout the lower units of the profile. However, they also proposed that the high apparent  $^{234}\text{U}$ - $^{238}\text{U}$  fractionations indicated that U was not easily removed from the ferruginous unit and that U would have been mostly retained by Fe oxyhydroxides. Because our measurements were made on isolated goethite of high purity, it is difficult to compare the results with those of a whole rock analysis. However, if U and Th were at any point mobilized throughout the Bahia profile, then the isochronous goethite He ages require that goethite aggregates acted as a robust closed system with respect to U and Th.

Several important questions arise regarding U and Th spatial variability within the goethite aggregates. U and Th are clearly not homogeneously distributed throughout the samples, although we do not well understand where or how U and Th are incorporated into the goethite aggregates. These parent elements are either incorporated into the goethite structure itself or adsorb onto mineral surfaces and are subsequently trapped into the crystal aggregate by overgrowth. Uranium adsorption onto goethite is an efficient process in groundwater systems (Andersson et al., 1998; Tricca et al., 2000; Giammer, 2001; Tricca et al., 2001), and it is possible that  $\text{UO}_2^{2+}$  adsorbs on goethite through inner-sphere surface complexes (Gabriel et al., 1998; Bargar et al., 1999; Giammer, 2001) or precipitates as minor amounts of U-phosphate, U-vanadate, or in another U-bearing supergene phase. Recent experimental investigation on uranium co-precipitation with synthetic iron oxides provides compelling evidence that U is incorporated into goethite structures and is not simply adsorbed onto mineral surfaces (Duff et al., 2002). The more limited aqueous mobility of Th in low-temperature groundwater suggests that any significant Th concentration may reflect inheritance of Th from primary minerals.

Thorium liberated during mineral dissolution would be immediately re-precipitated in situ.

Although the XRD of these samples indicated that they were high purity iron hydroxide, the possibility remains that U and Th precipitate into separate phases on a very small spatial scale. If so, then the goethite aggregate may simply act as a  $^4\text{He}$  carrier. Since U and Th decay series  $\alpha$  particles are ejected  $\sim 15 \mu\text{m}$  from their parent nuclei, it would be possible for most  $^4\text{He}$  to reside in goethite surrounding small ( $\sim \mu\text{m}$ ) autunite, tobernite, or other U/Th bearing inclusions. This would not violate the dating technique as long as: (1) the radiogenic helium is quantitatively sampled and analyzed with the parent nuclides; (2) the parent phase contemporaneously precipitated with the goethite; and (3) the parent phase does not contain inherited  $^4\text{He}$ . If goethite sufficiently retains implanted  $^4\text{He}$ , it would be of little consequence that parent and daughter nuclides reside in separate phases. Future studies using trace element probe analysis and synchrotron-based spectroscopic techniques (XAFS, XANES, etc.) will help identify the site and speciation of parent nuclides in aggregated goethite.

A significant difference among the samples is the high Th contents of near surface samples from the N4E *canga*. Although the goethite in these samples is visually pure, it is difficult to ascertain that these iron hydroxides precipitated directly from solution in open cavities, which would less likely incorporate detrital mineral impurities. The complexity of the processes occurring in the near surface environment, where biologic processes and the possibility of contamination by detrital and aeolian components strongly dominate mineral precipitation, may account for the high Th contents in these samples.

All of our He age calculations assume secular equilibrium among U-series daughters. This is clearly an oversimplification. Ground waters have  $^{234}\text{U}/^{238}\text{U}$  activity ratios that are usually  $>1$  (Coward et al., 1978; Osmond and Coward, 1992), and it is likely that goethites will precipitate with this elevated ratio. Similarly, it seems likely that the initial  $^{230}\text{Th}/^{238}\text{U}$  ratio of void-filling goethites precipitated directly from solution is  $\sim 0$ . Although initial disequilibrium will have a minor effect upon  $\sim$ several Ma He ages, the effects can be large in younger samples. Bender (1973) provides formulae for computing He ingrowth under these conditions. Excesses of  $^{234}\text{U}$  yield anomalously old ages, while deficits of  $^{230}\text{Th}$  yield anomalously young ages. For example, an initial  $^{234}\text{U}/^{238}\text{U}$  ratio of 1.1 and  $^{230}\text{Th}/^{238}\text{U}$  of zero yields an  $\sim 5\%$  underestimate of age at 1 Ma,  $\sim 0.6\%$  at 10 Ma, and  $\sim 0.05\%$  at 100 Ma (Bender, 1973; Farley et al., 2002). Without additional knowledge of the initial state of U series disequilibrium, the magnitudes of these effects set the minimum uncertainties to be expected for goethites of those ages. Although we can assume initial activity ratios, groundwater variability in  $^{234}\text{U}/^{238}\text{U}$  limits the ability to reliably date young goethites ( $<500$  ka) by the (U-Th)/He method.

## 6. STEPWISE DEGASSING EXPERIMENTS—RESULTS

Results of the stepped-heating diffusion experiments are given in Table 3 and presented as Arrhenius plots ( $\ln(D/a^2)$  vs.  $10^4/T$ ) in Figures 2 and 3 and ratio evolution diagrams in Figure 4. The experiments were conducted on proton-irradiated aliquots of samples 114 and 111.2. Due to the natural high  $^4\text{He}$  concentrations and

Table 3. Stepwise degassing results.

Step	T (°C)	t (hr)	<sup>3</sup> He (× 10 <sup>6</sup> atoms)	(+/-)	<sup>4</sup> He (× 10 <sup>9</sup> atoms)	(+/-)	Step	T (°C)	t (hr)	<sup>3</sup> He (× 10 <sup>6</sup> atoms)	(+/-)	<sup>4</sup> He (× 10 <sup>9</sup> atoms)	(+/-)
BAH-F124-114 (11.1mg)							BAH-F124-111.2 (3.4 mg)						
1	50	5	0.29	0.02	BDL	BDL	1	50	5	0.95	0.02	BDL	BDL
2	65	5	1.20	0.03	BDL	BDL	2	65	5	2.27	0.03	BDL	BDL
3	80	4	2.50	0.03	BDL	BDL	3	80	4	2.29	0.03	BDL	BDL
4	100	2	3.93	0.04	BDL	BDL	4	100	2	1.79	0.02	0.8	0.0
5	125	2	18.14	0.09	3.2	0.0	5	125	2	3.50	0.04	3.1	0.0
6	150	1	20.18	0.09	14.1	0.1	6	150	1	2.66	0.03	8.1	0.0
7	175	1	30.47	0.13	110.8	0.1	7	175	1	3.78	0.05	40.8	0.0
8	200	1	37.21	0.13	610.8	0.1	8	200	1	4.77	0.05	263.5	0.1
9	200	1	21.55	0.10	634.5	0.1	9	200	1	2.61	0.03	285.5	0.1
10	200	1	18.83	0.10	719.8	0.1	10	200	1	2.08	0.04	319.3	0.1
11	190	1	8.97	0.06	344.4	0.1	11	190	1	0.95	0.02	150.4	0.0
12	180	2	7.51	0.05	283.6	0.1	12	180	2	0.79	0.02	112.5	0.1
13	170	3	4.42	0.04	155.0	0.0	13	170	3	0.47	0.01	64.3	0.0
14	160	3	1.77	0.03	59.1	0.0	14	160	3	0.14	0.01	21.0	0.0
15	150	4	0.82	0.02	28.5	0.0	15	150	4	0.04	0.01	9.5	0.0
16	140	5	0.30	0.02	11.5	0.0	16	140	5	0.02	0.01	3.0	0.0
17	175	4	9.75	0.05	402.7	0.1	17	175	4	0.75	0.02	128.5	0.1
18	195	3	39.40	0.15	1874.3	0.2	18	195	3	3.49	0.03	821.8	0.1
19	205	2	57.77	0.15	2932.9	0.1	19	205	2	5.31	0.04	1315.6	0.1
20	210	1	41.76	0.11	2178.4	0.1	20	210	1	4.02	0.04	960.6	0.1
21	215	1	56.92	0.16	3021.5	0.1	21	215	1	5.45	0.05	1323.5	0.1
22	220	1	71.19	0.18	3787.7	0.2	22	220	1	7.26	0.05	1747.3	0.2
23	225	1	82.69	0.19	4471.8	0.2	23	225	1	9.69	0.06	2235.2	0.1
24	230	1	91.08	0.20	4974.9	0.2	24	230	1	12.36	0.06	2787.3	0.1
25	235	1	93.48	0.19	5050.4	0.2	25	235	1	15.18	0.08	3357.0	0.1
26	240	1	95.10	0.20	5093.9	0.2	26	240	1	17.49	0.09	3926.3	0.2
27	245	1	89.31	0.19	4636.9	0.2	27	245	1	19.35	0.08	4230.9	0.2
LS	~1300	0.5	277.89	0.33	14678.0	0.4	LS	~1300	0.5	81.45	0.20	24272.6	0.5
Total			1184.4		56078.5		Total			231.9		52645.1	

LS = last step, BDL = below detection limit.

The stepwise <sup>3</sup>He and <sup>4</sup>He degassing results used to calculate diffusion coefficients shown in Fig. 2 for Bahia goethite samples 114 and 111.2. Uncertainties in atomic abundance are reported at the 95% confidence level. All temperatures were controlled to better than 1 °C. LS = last step, BDL = below detection limit.

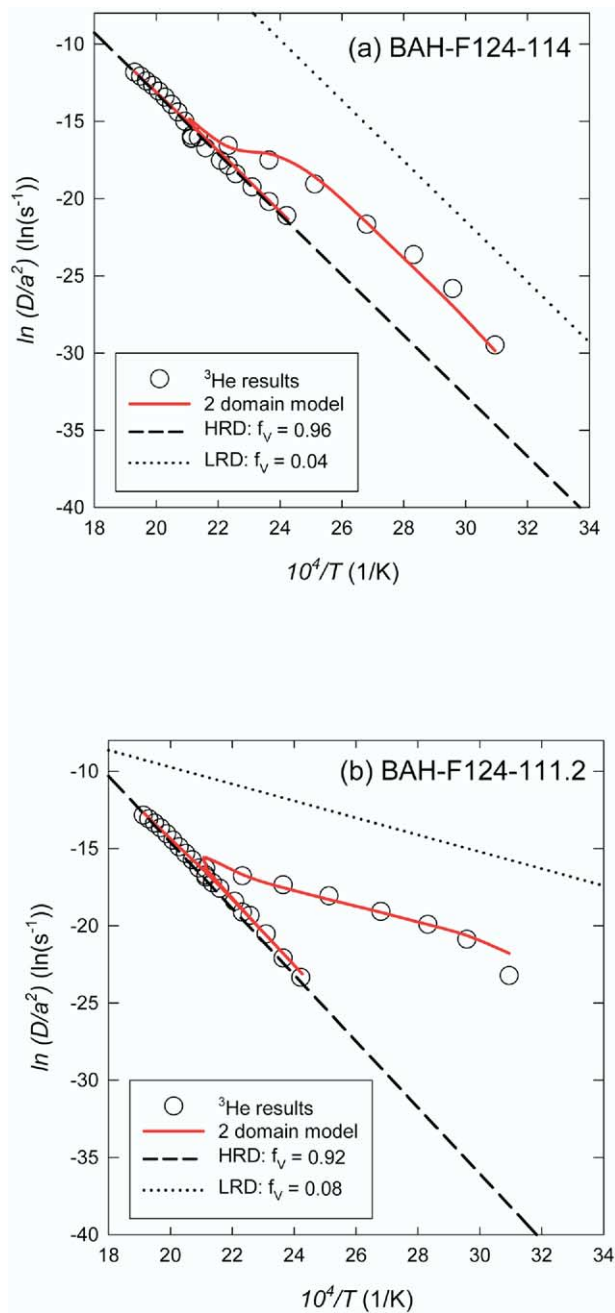


Fig. 2.  $^3\text{He}$  Arrhenius plots for (a) BAH-F124-114 and (b) BAH-F124-111.2. Open circles are values calculated from release fractions of proton-induced  $^3\text{He}$  according to Fechtig and Kalbitzer (1966). The dashed lines are the least squares regressions through the HRD of each sample. The solid curves are the two-domain models used to construct the curves shown in Figure 4 and summarized in Table 4. For reference, the dotted lines are the diffusion parameters of the LRD and  $f_v$  denotes the volume fraction of each domain used to construct the two-domain models.

low  $^3\text{He}/^4\text{He}$  ratios of these samples, the proton irradiation effectively generated a purely synthetic distribution of  $^3\text{He}$  in samples containing a natural distribution of *only*  $^4\text{He}$ . Spallogenic helium produced via proton bombardment has a  $^4\text{He}/^3\text{He}$  ratio of  $\sim 10$ , contributing a negligible component to the  $^4\text{He}$  budget of each

sample. For this reason, we can consider the experimental results of each isotope separately, as each should provide distinct information about the sample (Shuster and Farley, 2004; Shuster et al., 2004). We present diffusion coefficients calculated from the measured release fractions of proton-induced  $^3\text{He}$  in Figure 2 and radiogenic  $^4\text{He}$  in Figure 3. Due to the possibility of diffusive rounding, values of  $\ln(D/a^2)$  calculated from  $^4\text{He}$  release fractions may not accurately

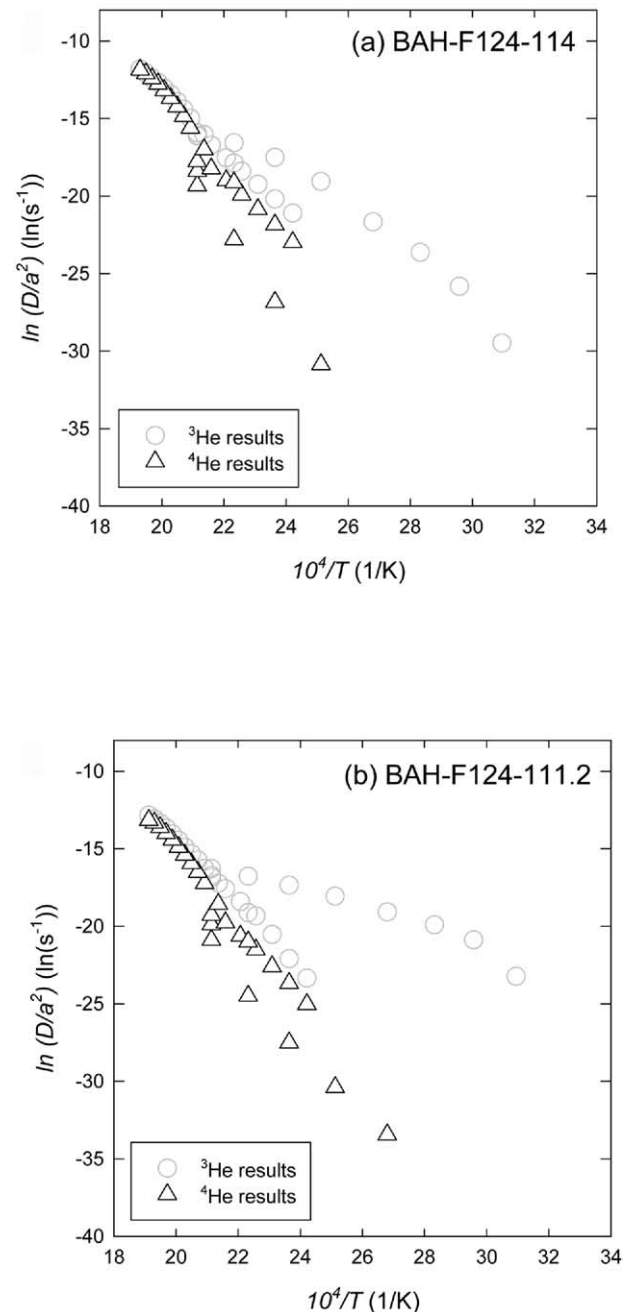


Fig. 3.  $^4\text{He}$  Arrhenius plots for (a) BAH-F124-114 and (b) BAH-F124-111.2. Triangles are values calculated from release fractions of radiogenic  $^4\text{He}$  according to Fechtig and Kalbitzer (1966). Also shown for reference as open circles are the  $^3\text{He}$  determined values presented in Figure 2.

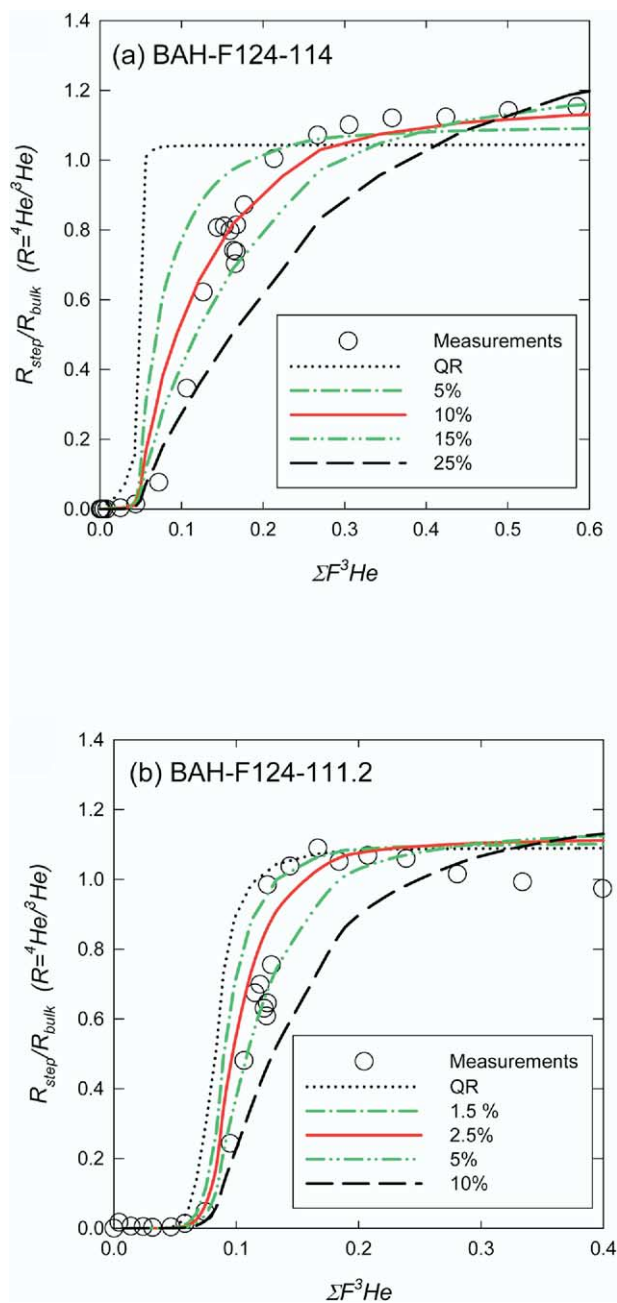


Fig. 4. Goethite  $^4\text{He}/^3\text{He}$  vs.  $\Sigma^3\text{He}$  Goethite ratio evolution diagrams for (a) BAH-F124-114 and (b) BAH-F124-111.2. Shown are measured isotope ratios for each release step,  $R_{\text{step}}$  ( $R = ^4\text{He}/^3\text{He}$ ), normalized to the bulk ratio  $R_{\text{bulk}}$  plotted vs. the cumulative  $^3\text{He}$  release fraction,  $\Sigma F^3\text{He}$ . Five two-domain diffusion models are shown for each sample with deficit gas fractions of the HRD indicated in the legend. QR denotes quantitative  $^4\text{He}$  retention in the HRD. The analytical uncertainties of the points are of order 5% (roughly twice the diameter of the points) and are excluded from the diagram for clarity. Note that the two figures are at different scales.

reflect diffusivity. We therefore concentrated on  $^3\text{He}$  to quantify helium diffusion coefficients and  $^4\text{He}$  to determine the degree of partial  $^4\text{He}$  retention. Note that the heating schedules of these experiments included both prograde (sequentially increasing) and retrograde (decreasing) steps.

## 6.1. Proton-Induced $^3\text{He}$ Diffusion Parameters

The most apparent feature of the  $^3\text{He}$  results is a break in slope occurring at  $\sim 180^\circ\text{C}$  that separates two distinct arrays (Fig. 2). The array of higher diffusivity was obtained from the initially derived gas, and amounts to 4 and 8% of the total  $^3\text{He}$  budgets of samples 114 and 111.2, respectively. Note that points on an Arrhenius plot are not weighted according to the amount of extracted gas. For example, although the higher diffusivity arrays have strong graphical representation, the steps cumulatively represent small proportions of the total  $^3\text{He}$  budgets.

This type of feature has been observed in other phases using both proton-induced  $^3\text{He}$  and radiogenic  $^4\text{He}$ , and suggests that multiple diffusion domains are present in the samples (Reiners and Farley, 1999; Reiners et al., 2004; Shuster et al., 2004). Although these data have important implications discussed further below, the arrays of lower diffusivity, representing the majority ( $>90\%$ ) of the extracted  $^3\text{He}$ , better characterize helium diffusivity in the bulk of the polycrystalline samples. These arrays have strong linear correlations between  $\ln(D/a^2)$  and  $1/T$  between  $145^\circ\text{C}$  and  $225^\circ\text{C}$  with correlation coefficients ( $R^2$ ) higher than 0.996 for each experiment. The correlations persist throughout retrograde temperature cycles indicating that (1) during those steps  $^3\text{He}$  is derived primarily from a single characteristic domain size, and (2) the assumed initial uniform  $^3\text{He}$  distribution is valid (Shuster and Farley, 2004; Shuster et al., 2004). Regressions through these data are shown as dashed lines in the Arrhenius plots (Fig. 2), and the diffusion parameters extracted from each regression are indicated in Table 4 as the *high retentivity domains* (HRD). Sample 114 results were qualitatively duplicated in a more coarsely conducted experiment (not presented) on a different aliquot of smaller physical aggregate size. In that experiment, both the overall shape of the Arrhenius plot, and the regression through the HRD were in excellent agreement with the results presented in Figure 2.

Goethite 111.2, as defined by the array of lower diffusivities, is slightly more helium retentive than sample 114. As discussed below, the two arrays have the following diffusion parameters:  $E_a = 162.8 \pm 2.4$  kJ/mol and  $\ln(D_0/a^2) = 26 \pm 0.6$   $\ln(\text{s}^{-1})$ ; and  $E_a = 178.4 \pm 2.6$  kJ/mol and  $\ln(D_0/a^2) = 28.3 \pm 0.6$   $\ln(\text{s}^{-1})$ , for samples 114 and 111.2, respectively. By assuming a diffusive length scale “ $a$ ” of  $0.5$   $\mu\text{m}$  for both samples (Fig. 1b and see Discussion), we can estimate the frequency factors  $D_0$  with which to compare these results to other phases commonly used for (U-Th)/He dating. We estimate the following values:  $\ln(D_0) = 6.2$  and  $\ln(D_0) = 8.5$   $\ln(\text{cm}^2/\text{s})$ , for samples 114 and 111.2, respectively. Durango apatite and FCT titanite each have comparable activation energies (148 and 183 kJ/mol, respectively), but lower frequency factors ( $\sim 3.4$  and  $\sim 4.1$   $\ln(\text{cm}^2/\text{s})$ , respectively; (Reiners and Farley, 1999; Farley, 2000)), indicating that the polycrystalline goethite is less helium retentive than these phases.

## 6.2. Radiogenic $^4\text{He}$ Diffusion Coefficients

Shown in Figure 3, the diffusion coefficients calculated from  $^4\text{He}$  are initially lower than those calculated from  $^3\text{He}$  and are also significantly lower than the HRD linear regressions discussed above and shown in Figure 2. For instance, in the 114

experiment, the early step at 100°C yielded a value of  $D/a^2$  that is a factor of  $1.2 \times 10^{-4}$  lower than the HRD  $^3\text{He}$  based extrapolation. However, as each experiment proceeded toward higher gas yields, the apparent  $\ln(D/a^2)$  coefficients calculated from each isotope became gradually convergent. At the highest temperatures and latest steps of each experiment, the results calculated from  $^3\text{He}$  become statistically indistinguishable from  $^4\text{He}$ . These features are expected if proton-induced  $^3\text{He}$  and radiogenic  $^4\text{He}$  have equivalent diffusivity in goethite and the natural  $^4\text{He}$  has a diffusively modified spacial distribution (Shuster and Farley, 2004; Shuster et al., 2004).

### 6.3. Ratio Evolution Diagrams

A  $^4\text{He}/^3\text{He}$  ratio evolution diagram ( $R_{step}/R_{bulk}$ , where  $R = ^4\text{He}/^3\text{He}$  vs. cumulative  $^3\text{He}$  release fraction,  $\Sigma F^3\text{He}$ ) is useful for constraining the spatial distribution of  $^4\text{He}$  in proton irradiated samples (Shuster and Farley, 2004). The measured ratio evolution diagrams for each experiment are shown in Figure 4. In each experiment, the values of  $R_{step}/R_{bulk}$  are very low when  $\Sigma F^3\text{He} < 0.1$  followed by a sharp and continuous increase to values that are more consistent with the bulk  $^4\text{He}/^3\text{He}$  ratio ( $R_{step}/R_{bulk} \sim 1$ ). The increase to higher values of  $R_{step}/R_{bulk}$  occurred more gradually for sample 114 than for sample 111.2. For instance,  $R_{step}/R_{bulk}$  of sample 114 increased from  $\sim 0$  to values  $\geq 1.0$  in the range of  $\Sigma F^3\text{He}$  from 0.04 to 0.30. The same occurred abruptly for sample 111.2 in the range of  $\Sigma F^3\text{He}$  from 0.07 to 0.12. Note that the high density of values at  $\Sigma F^3\text{He} \sim 0.15$  were determined during retrograde heating cycles in each experiment.

Once each of the stepped experiments evolved to  $R_{step}/R_{bulk} \geq 1.0$ , the measured ratios remained relatively constant. However, whereas the last few steps in the sample 114 experiment continually increased, the last few steps of sample 111.2 slightly but significantly decreased from a maximum value obtained when  $\Sigma F^3\text{He} \sim 0.2$ . Most of the information about a  $^4\text{He}$  distribution is expressed at low gas yields ( $\Sigma F^3\text{He} < 0.4$ ) of a single domain ratio evolution diagram (Shuster and Farley, 2004). At low yields the effects of diffusive loss are most pronounced. For this reasons we focused on the  $^4\text{He}/^3\text{He}$  ratios when  $\Sigma F^3\text{He} < 0.4$  to interpret Figure 4.

### 6.4. Helium Retentivity

Because supergene weathering products likely have isothermal histories (precipitation and residence at low temperatures), the closure temperature ( $T_c$ ) is inappropriate for characterizing helium retentivity. Instead, we borrow a simple model of isothermal diffusive loss and radiogenic in-growth, presented by Ozisik (1989) and modified for He dating as presented in Wolf et al. (1998). For given functions of  $D(T)/a^2$ , plots of isothermal holding time ( $t$ ) vs. expected He age ( $t'$ ) can be calculated to evaluate the effect of diffusive  $^4\text{He}$  loss upon a He age.

In Figure 5 we present helium retention factors (curves plotted as He age/holding time ( $t'/t$ )) for three isothermal temperatures as functions of isothermal holding times. The calculations are shown for the HRD diffusivity functions  $D(T)/a^2$  for the two samples. Note that here we discuss only the curves and that the points corresponding to “corrected ages”

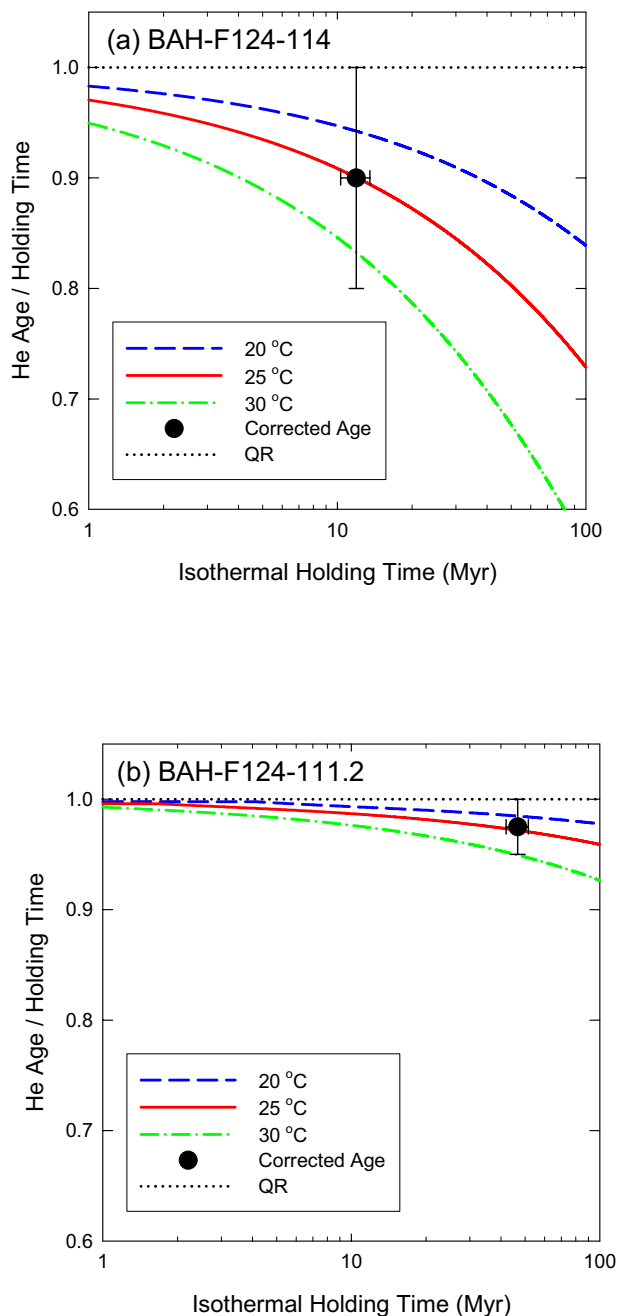


Fig. 5.  $^4\text{He}$  retention curves. Helium-4 retention curves for (a) BAH-F124-114 and (b) BAH-F124-111.2. Shown as solid curves are  $^4\text{He}$  retentivity factors (the He age divided by an isothermal holding time) plotted vs. isothermal holding time in Myrs. Three curves were calculated for 20, 25 and 30°C according to the HRD diffusion parameters summarized in Table 4 and the formulation of Wolf et al. (1998). Also plotted are the independently determined corrected He ages and HRD retentivity factors (i.e., 1—deficit gas fraction) for each sample. QR denotes quantitative  $^4\text{He}$  retention in the HRD.

will be considered in a later section (see He age corrections). The curves in Figure 5 clearly illustrates that the helium retentivity of the two samples is different. For instance, at 25°C after 10 Myrs the HRD in sample 114 would have a deficit gas fraction of 10% (He age/holding time = 0.90), whereas the

HRD in sample 111.2 would have a deficit gas fraction of only ~1%. Deficit gas fractions are defined as  $(N_{uniform} - N_o)/N_{uniform}$ , where  $N$  is the total amount of  $^4\text{He}$  in a diffusively modified profile ( $N_o$ ) and a uniform profile ( $N_{uniform}$ ) resulting from quantitative retention (Shuster and Farley, 2004).

The curves in Figure 5 also illustrate that helium retention in polycrystalline goethite is strongly temperature dependent. Future studies involving goethite will require careful sample selection and consideration of thermal conditions. For instance, these goethites would be susceptible to diffusive  $^4\text{He}$  loss associated with intense solar heating and episodic forest fires if they were located at the surface. The results clearly indicate that  $^4\text{He}$  is not expected to be quantitatively retained in the two Bahia samples, but that significant fractions of gas should be retained. Although the curves presented in Figure 5 are useful for predicting an expected degree of diffusive loss, a detailed interpretation of the ratio evolution diagrams should permit quantification of the deficit gas fraction.

## 7. STEPWISE DEGASSING EXPERIMENTS—DISCUSSION

Under the assumption that proton-induced  $^3\text{He}$  was uniformly produced and reflects all of the diffusion domains that may be present in each sample, the interpretation of the ratio evolution diagrams (Fig. 4) yields a quantitative description of helium diffusion from all of the domains in the samples. Likewise, the interpretation of the  $^3\text{He}$  diffusion experiments and the extraction of diffusion parameters from them rely upon our anticipation of multiple diffusion domain sizes in the polycrystalline goethite aggregates. In this sense, our treatment of the  $^3\text{He}$  release data are analogous to and based on previous work using neutron-induced  $^{39}\text{Ar}$  in feldspars (Lovera et al., 1989; Lovera et al., 1991, among others) and natural  $^4\text{He}$  in titanite (Reiners and Farley, 1999) and zircon (Reiners et al., 2004) to identify multiple diffusion domains.

The distinct arrays and breaks in slope observed in Figure 2 preclude the possibility that a single diffusive length-scale (i.e.,  $a$  in  $D/a^2$ ) characterizes helium diffusion in either sample. The presence of more than a single diffusion domain complicates a diffusion experiment. Gas initially extracted from a distribution of diffusion domains will be a mixture: a larger fraction from less retentive domains and a smaller fraction from more retentive domains. Since the mathematics of Fechtig and Kalbitzer (1966) assume that the gas is derived from a single domain, the presence of a small volume fraction of low retentivity domains will result in values of  $D/a^2$  that are initially higher than the mean for a given temperature.

If the diffusivity,  $D(T)$ , is the same throughout all domains, each would share common activation energy  $E_a$  and therefore a common slope on an Arrhenius plot. The origin of initially higher values of  $D/a^2$ , then, would simply be the dominance of a smaller domain radius,  $a$ , at that stage of the experiment. Alternatively, if the domains have significantly different  $E_a$ , the slopes of the arrays could be distinct. As an experiment proceeds, gas is progressively extracted from all diffusion domains. The less retentive domains will exhaust first, causing a transition in the calculated  $D/a^2$  values to those associated with the more retentive domains.

It is important to note that the exact shape of an Arrhenius plot is a strong function of the heating schedule used. For

instance, a diffusively modified distribution or multiple diffusion domain sizes can cause retrograde cycles to appear different from prograde steps (Lovera et al., 1989; Lovera et al., 1991). Indeed, these are reasons for including retrograde cycles in our experiments (see Table 3). A successful multiple-domain model should reproduce the shape of an Arrhenius plot in detail. For this reason, we constructed models with the same heating schedule as used in the experiments.

### 7.1. Two-Domain Model

To describe the  $^3\text{He}$  release patterns for each experiment, we developed two-domain models to reproduce the observed  $^3\text{He}$  Arrhenius plots. Since the bulk of each sample (the HRD) was well characterized by the arrays of lower diffusion coefficients, a relatively narrow range in HRD diffusion parameters was permissible in the models. And, since the two arrays in each experiment were quite distinct, the volume fractions of the LRD were well approximated by the cumulative  $^3\text{He}$  release fraction up to the point the arrays converge (4 and 8% as discussed above). Therefore, the two-domain models each effectively had only two free parameters,  $E_a$  and  $\ln(D_0/a^2)$  for the LRD. However, diffusion coefficients calculated throughout the experiment are somewhat dependent upon the LRD, and the extraction of the HRD diffusion parameters from Figure 2 requires consideration of all domains present. Although more complicated models involving more than two domains or a continuum of domains could be developed, the highly simplified two-domain models are sufficient to explain the  $^3\text{He}$  observations. As such, we must emphasize that each two-domain model is a non-unique solution.

The models were calculated by assuming that the  $^3\text{He}$  distributions were initially uniform within two distinct populations of domains, and gas was not permitted to exchange between domains. Release fractions from the HRD and LRD were calculated separately using the heating schedules of each experiment, then summed at each step to yield a two-domain model  $^3\text{He}$  release pattern. The calculations were iterated by adjusting  $E_a$  and  $\ln(D_0/a^2)$  for the LRD until each model was consistent with the observed Arrhenius plots shown in Figure 2.

The best-fit two-domain models are shown in Figure 2 as solid curves. We found model parameters that successfully reproduce the shapes of the Arrhenius plots and that the activation energies of the LRD are well approximated by the slopes of the LRD arrays. We also found that the best-fit model diffusion parameters for the HRD were well approximated by the independent linear regressions through the arrays of lower diffusivity (see above). This is primarily due to the substantial difference in diffusivity between the two domains. For reference, the LRD and HRD diffusion parameters are plotted as dotted and dashed lines, respectively in Figure 2 and also summarized in Table 2.

Under the two-domain model, the  $^3\text{He}$  Arrhenius plots indicate that the helium diffusion in the LRD behaves quite differently between sample 114 and 111.2. Although both of the LRD are effectively non-helium-retentive over geologic time, their relative proportions are important characteristics of each sample. Although the diffusion properties of each LRD may provide insight into what the domains represent (see below), the excellent agreement between models and observations in

Figure 2 does not rigorously prove bidomainality. Regardless of their physical significance, the two-domain models provide a framework which can be used to interpret the  $^4\text{He}/^3\text{He}$  ratio evolution diagrams.

## 7.2. Quantifying Deficit Gas Fractions

If the spatial distribution of  $^4\text{He}$  within the goethites can be constrained, then the deficit gas fraction can be quantified. The deficit gas fraction is useful for correcting an absolute He age for diffusive  $^4\text{He}$  loss.

Given the two-domain models summarized in Table 2, and using the methods described by Shuster and Farley (2004), we simulated the expected  $^4\text{He}$  distributions within the samples under different isothermal conditions over geologic time. We assumed that the diffusivity of proton-induced  $^3\text{He}$  and radiogenic  $^4\text{He}$  is equivalent in these samples, although our results are not strongly sensitive to this assumption (Shuster et al., 2004). Each simulation was required to result in the observed He ages (10.7 and 42.6 Ma for sample 114 and 111.2, respectively), and each corresponds to a different deficit gas fraction.

The model  $^4\text{He}$  distributions were first calculated for the HRD of each sample, and then passed through a simulated degassing experiment to produce a set of  $^4\text{He}$  release fractions. Because the LRD of each sample are effectively non-retentive, their presence could be ignored in the profile calculating step. For instance, any radiogenic  $^4\text{He}$  produced within the LRD would be “immediately” lost on a geologic timescale. To simulate ratio evolution diagrams, a uniform distribution of  $^3\text{He}$  within both domains was also passed through the same simulated degassing experiment from which model  $^4\text{He}/^3\text{He}$  could be calculated.

The  $^4\text{He}$  modeling results are presented as curves in Figure 4. Several features in the models of both samples are immediately apparent. First, the models successfully reproduce the low  $^4\text{He}/^3\text{He}$  ratios at the beginning of each experiment. This is clearly controlled by the relative proportion of the  $^3\text{He}$ -only containing LRD and illustrates how well those proportions are constrained. Second, both sets of models successfully reproduce the gradual and sharp rises in  $^4\text{He}/^3\text{He}$  for sample 114 and 111.2, respectively, each followed by nearly invariant ratios.

Although the models do not perfectly match the data, we can use them to place strong limits on the degrees of diffusive  $^4\text{He}$  loss for each sample. For instance, if the models are accurate, sample 114 has retained >75% of its  $^4\text{He}$ , and 111.2 has retained >90%. We can also rule out the possibility that either sample quantitatively retained  $^4\text{He}$ . Despite significant scatter in the data, particularly during the retrograde cycles during which gas yields were low, we find that a 10% and a 2.5% deficit gas fraction best reproduces the results of sample 114 and 111.2, respectively.

## 7.3. He Age Corrections

Assuming that both domains are inherent to each sample and that radiogenic  $^4\text{He}$  was naturally produced uniformly throughout each domain, the modeling results suggest that two components must be quantified and added back into the  $^4\text{He}$  budget of each sample to correct its (U-Th)/He age. These components are the  $^4\text{He}$  quantitatively lost from the non-retentive LRD and

the deficit gas fraction of  $^4\text{He}$  diffusively lost from the HRD of each sample.

Using a HRD deficit gas fraction of 10% for sample 114, we can correct the measured  $^4\text{He}$  concentration for partial diffusive loss from those domains, where corrected He content = measured content  $\div$  (1 - deficit gas fraction) (Shuster and Farley, 2004). This corrects the measured He age (10.7 Ma) to 11.8 Ma. The LRD represents 4% of the total  $^3\text{He}$  budget. If  $^4\text{He}$  produced in the LRD was quantitatively lost over geologic time, a similar correction brings the final corrected He age to 12.3 Ma. If we conservatively assume 100% uncertainty on each correction, the final age of sample 114 is  $12.3 \pm 1.6$  Ma. For BAH-F124-111.2 we estimate the HRD deficit gas fraction to be ~2.5% and the fraction of gas lost from the LRD to be 8%. Applying both corrections and assuming 100% uncertainty on each brings the measured He age of 42.6 Ma to a final corrected age of  $47.5 \pm 4.9$  Ma for sample 111.2.

It is difficult to estimate the actual uncertainty associated with the two corrections we describe above. Uncertainties associated with measured release fractions, linear Arrhenius regressions and the fits of  $^3\text{He}$  Arrhenius models, individual He, U and Th measurements, raw aliquot He age reproducibility, U series secular dis-equilibrium and the fits of ratio evolution models all contribute to the final uncertainty of a corrected He age. In these types of samples, we can easily measure [ $^4\text{He}$ ], [U] and [Th] to better than ~1% analytical precision, and we find good He age reproducibility (Table 1). However, the uncertainty in a weathering product He age will be dominated by the uncertainty in He loss corrections described above. By assuming 100% uncertainty, we place a very conservative estimate of the uncertainty in a corrected He age.

An important caveat to the HRD correction is the possibility that an even higher retentivity domain exists in the sample but is not interrogated until the final total fusion of the sample at ~1300°C (last step, Table 3). Such a domain would be unrecognized in Figure 2. However, since a domain of sufficiently distinct retentivity would likely require distinct chemistry, the domain may have a different U, hence  $^4\text{He}$  content. Such a scenario could be recognized by the ratio evolution diagram if the total fusion step had a sufficiently different  $^4\text{He}/^3\text{He}$  than the rest of the sample. Rigorously, the HRD correction is only valid for the fraction of the sample interrogated by the Arrhenius plot. We have implicitly assumed that domains of higher retentivity than the HRD do not exist in either sample.

The magnitude of the above corrections illustrates the limitation of this dating technique and emphasizes the value of performing a stepped degassing analysis on a sample. Although more labor intensive than determining a basic (U-Th)/He age, the ability to recognize non-quantitative  $^4\text{He}$  retention and apply age corrections improves the accuracy of the precipitation ages.

## 7.4. Internal Consistency and Mean Temperature

If the corrected He ages represent the true precipitation age of each sample, the pair of Bahia goethites provides a test for internal consistency. Goethite samples 114 and 111.2 were located 3 m from one another in the weathering profile. For at least the duration of the younger sample's existence, this pair must have shared a common thermal history. We a priori expect

Table 4. Two-domain model diffusion parameters

Sample	$f_V$	$E_a$ (kJ/mol)	(+/-)	$\ln(D_0/a^2)$ $\ln(s^{-1})$	(+/-)	$R^2$
BAH-F124-114						
HRD	0.96	162.8	2.4	26.0	0.6	0.997
LRD	0.04	162.8	—	37.3	—	—
BAH-F124-111.2						
HRD	0.92	178.4	2.6	28.3	0.6	0.996
LRD	0.08	45.6	—	1.3	—	—

HRD is “high retentivity domains” and LRD is “low retentivity domains”. Standard errors in the regression statistics are reported for the HRD at the 95% confidence level.

that mean temperatures these samples experienced was controlled by the mean annual air temperature of the region, 23°C. Although the mean temperature over the last ~40 Myrs is not well known, the samples should have remained well below 35°C throughout their existence.

Using  $^3\text{He}$  derived diffusion parameters for the HRD of each sample, the production/diffusion model predicts a He age and concentration profile for a given isothermal holding time and temperature (Fig. 5, curves). The diffusion-corrected He ages and the HRD deficit gas fractions determined from Figure 4 provide us the ability to superimpose each sample on the curves, shown as solid circles. Each sample indicates a physically reasonable residence temperature of ~25°C. The agreement between these results and the actual mean temperature of 23°C is significant, indicating that the diffusive loss corrections, the LRD corrections, and the temperature extrapolations of the  $^3\text{He}$  determined functions  $D(T)/a^2$  are not severely inaccurate. Failure of this test would indicate inaccuracy in any of the above.

### 7.5. Physical Significance of Diffusion Domains

The physical significance of the apparent diffusion domains remains an unanswered question about these samples. Unlike single euhedral crystals, in fine grained polycrystalline material the physical identity of diffusion domains is unclear. The diffusion domain(s) may correspond to individual FeOOH crystals of various sizes, amorphous intergranular media, or even the bulk aggregate geometry in the case of the HRD.

If the bulk aggregate geometry defines the high retentivity diffusion domains, then we expected to find a difference between the two diffusion experiments performed on BAH-F124-114. Because we analyzed an aliquot ~1 mm in chip radius and one ~200  $\mu\text{m}$  in radius, a difference in  $\ln(D_0/a^2)$  of ~3 natural log units would be expected. Although the aliquots were not perfectly spherical, a difference in  $\ln(D_0/a^2)$  of 3  $\ln$  units should be detectable despite the coarseness with which the 200  $\mu\text{m}$  experiment was conducted. We found no significant difference between the HRD regressions of each Arrhenius plot. This implies that the characteristic domains size,  $a$ , is significantly smaller than the bulk aggregate geometry, and common to both aliquots.

The LRD diffusion parameters of sample 111.2 are very different from the rest of the sample, and also very different from the LRD of sample 114. Although both of the LRD diffuse helium rapidly, the very low activation energy (46

kJ/mol) of the LRD of sample 111.2 indicates those domains are fundamentally distinct from the rest of the sample. Previous work with Mn oxides revealed the residence of  $^{40}\text{Ar}$  in domains thought to be very low retentivity intergranular regions. This intergranular domain hosts atmospheric  $^{40}\text{Ar}$ ,  $^{38}\text{Ar}$ , and  $^{36}\text{Ar}$ , but does not contain any significant radiogenic ( $^{40}\text{Ar}^*$ ) or nucleogenic gas (e.g.,  $^{37}\text{Ar}$  and  $^{39}\text{Ar}$ ). The volume of intergranular space determines the density of the sample and depends on the packing of the acicular or rod-shaped hollandite and goethite micro-crystallites. In addition, the retentivity of the intergranular space may vary locally, depending on crystallite shape, size, and packing density. If this is also true of helium in polycrystalline goethite, we should expect variability in the relative proportions of HRD and LRD between samples related to the packing density of aggregated crystals and crystallinity index. Future studies involving careful characterization of sample crystallinity and trace chemical impurities are required to fully understand the physical significance of the apparent domains.

### 7.6. General Extrapolation of Goethite Diffusion Parameters

Despite general agreement between the measured diffusion parameters for the two goethites, every polycrystalline goethite aggregate may behave differently. The diffusion domain size distribution as well as an aggregate’s physical characteristics such as crystallinity and morphology may vary significantly from sample to sample. Until the relevant parameters that control  $^4\text{He}$  diffusion in goethite have been identified and quantified, it may be necessary to perform an irradiation/diffusion experiment to accurately interpret or correct goethite He ages.

## 8. CONCLUSIONS

Goethite (U-Th)/He dating is a viable weathering geochronometer. We found (U-Th)/He ages determined on aliquots of polycrystalline goethite to be reproducible despite variability in U and Th content. Stepwise degassing analyses of proton-irradiated aliquots have revealed the following about two polycrystalline goethites: (1)  $^3\text{He}$  does not reside in a single diffusion domain, but resides in at least two distinct domains; (2) two-domain models constrain the functions  $D(T)/a^2$  for each domain and the relative proportions of  $^3\text{He}$  located in each; (3) ratio evolution diagrams reveal diffusive  $^4\text{He}$  distributions

within the samples; and (4) the two samples retain  $^4\text{He}$  to different degrees.

Although  $^4\text{He}$  is not quantitatively retained in aggregated polycrystalline goethites, the magnitude of diffusive loss is not prohibitive. The ability to rigorously quantify diffusive-loss corrections by using the proton-irradiation  $^4\text{He}/^3\text{He}$  method enables goethite precipitation ages to be determined.

The widespread distribution of goethite in weathering profiles on Earth and possibly other terrestrial planets and the feasibility of dating goethite by the (U-Th)/He method opens new opportunities for quantifying water-rock interaction in the geological past. Application of goethite (U-Th)/He dating, if combined with stable isotope studies (O, H, and C), may provide a feasible mechanism for generating a nearly continuous paleoclimatic curve for continental areas suitable for comparison with the record preserved in oceanic reservoirs.

*Acknowledgments*—We thank L. Hedges and C. Paine for sample preparation and J. Sistierson and E. Cascio for their expertise with the proton irradiation. We thank P. Reiners and an anonymous reviewer for their constructive comments on the manuscript. This work was supported by the National Science Foundation and UQ-AGES (University of Queensland Argon Geochronology in Earth Sciences) Laboratories. D.L.S. was supported by a N.S.F. Graduate Research Fellowship.

*Associate editor:* T. M. Harrison

## REFERENCES

- Anand R. R., and Paine M. (2002) Regolith geology of the Yilgarn Craton, Western Australia: implications for exploration. *Aus. J. Earth Sci.* **49** (1), 3–162.
- Andersson P. S., Porcelli D., Wasserburg G. J., and Ingri J. (1998) Particle transport of (super 234) U- (super 238) U in the Kalix River and in the Baltic Sea. *Geochim. Cosmochim. Acta* **62** (3), 385–392.
- Baehr R., Lippolt H. J., and Wernicke R. S. (1994) Temperature-induced  $^4\text{He}$  degassing of specularite and botryoidal hematite; a  $^4\text{He}$  retentivity study. *J. Geophys. Res., B, Sol. Earth Planets* **99**(9), 17,695–17,707.
- Bargar J. R., Persson P., and Brown G. E. Jr. (1999) Outer-sphere adsorption of Pb(II)EDTA on goethite [Monograph] *Geochemistry in aqueous systems; a special issue in honor of Werner Stumm. Geochim. Cosmochim. Acta* **63** (19–20), 2957–2969.
- Bender M. (1973) Helium-Uranium dating of corals. *Geochim. Cosmochim. Acta* **37**, 1229–1247.
- Bird M. I., and Chivas A. R. (1993) Geomorphic and palaeoclimatic implications of an oxygen-isotope chronology for Australian deeply weathered profiles. *Aus. J. Earth Sci.* **40** (4), 345–358.
- Braucher R., Bourles D. L., Brown E. T., Colin F., Muller J.-P., Braun J. J., Delaune M., Edou Minko A., Lescouet C., Raisbeck G. M., and Yiou F. (2000) Application of in situ-produced cosmogenic (super 10) Be and (super 26) Al to the study of lateritic soil development in tropical forest; theory and examples from Cameroon and Gabon. *Chem. Geol.* **170** (1–4), 95–111.
- Braucher R., Bourles D. L., Colin F., Brown E. T., and Boulange B. (1998) Brazilian laterite dynamics using in situ-produced (super 10) Be. *Earth Planet. Sci. Lett.* **163** (1–4), 197–205.
- Brown E. T., Bourles D. L., Colin F., Sanfo Z., Raisbeck G. M., and Yiou F. (1994) The development of iron crust lateritic systems in Burkina Faso, West Africa examined with in-situ-produced cosmogenic nuclides. *Earth Planet. Sci. Lett.* **124** (1–4), 19–33.
- Cowart J. B., Kaufman M. I., and Osmond J. K. (1978) Uranium-isotope variations in groundwaters of the Floridan Aquifer and Boulder Zone of South Florida. *J. Hydrol.* **36** (1–2), 161–172.
- Dammer D., Chivas A. R., and McDougall I. (1996) Isotopic dating of supergene manganese oxides from the Grootte Eylandt Deposit, Northern Territory, Australia. *Econ. Geol. Bull. Soc. Econ. Geol.* **91** (2), 386–401.
- Dammer D., McDougall I., and Chivas A. R. (1999) Timing of weathering-induced alteration of manganese deposits in Western Australia; evidence from K/Ar and (super 40) Ar/ (super 39) Ar dating. *Econ. Geol. Bull. Soc. Econ. Geol.* **94** (1), 87–108.
- Dequincey O., Chabaux F., Clauer N., Liewig N., and Muller J. P. (1999) Dating of weathering profiles by radioactive disequilibria; contribution of the study of authigenic mineral fractions. *Comptes Rendus de l'Academie des Sciences, Serie II. Sciences de la Terre et des Planetes* **328** (10), 679–685.
- Dequincey O., Chabaux F., Clauer N., Sigmarsson O., Liewig N., and Leprun J. C. (2002) Chem. mobilizations in laterites; evidence from trace elements and  $^{238}\text{U}$ - $^{234}\text{U}$ - $^{230}\text{Th}$  disequilibria. *Geochim. Cosmochim. Acta* **66** (7), 1197–1210.
- Diakonov I., Khodakovskiy I., Schott J., and Sergeeva E. (1994) Thermodynamic Properties of Iron-Oxides and Hydroxides. 1. Surface and Bulk Thermodynamic Properties of Goethite (Alpha- Feooh) up to 500-K. *Eur. J. Min.* **6** (6), 967–983.
- Duff M. C., Coughlin J. U., and Hunter D. B. (2002) Uranium coprecipitation with iron oxide minerals. *Geochim. Cosmochim. Acta* **66** (20), 3533–3547.
- Farley K. A. (2000) Helium diffusion from apatite: general behavior as illustrated by Durango fluorapatite. *J. Geophys. Res.* **105**, 2903–2914.
- Farley K. A. (2002) (U-Th)/He Dating: Techniques, Calibrations, and Applications. In *Rev. in Mineralogy and Geochemistry: Noble Gases in Geochemistry and Cosmochemistry* (eds. D. Porcelli, C. J. Ballentine and R. Wieler), Vol. 47 pp. 819–844.
- Farley K. A., Kohn B. P., and Pillans B. (2002) (U-Th)/He dating of Pleistocene zircon and apatite: A test case from the Rangitawa tephra, North Island, New Zealand. *Earth Planet. Sci. Lett.*, **201** (1), 117–125.
- Farley K. A., Wolf R. A., and Silver L. T. (1996) The effects of long alpha-stopping distances on (U-Th)/He ages. *Geochim. Cosmochim. Acta* **60**, 4223–4229.
- Fechtig H. and Kalbitzer S. (1966) The diffusion of argon in potassium-bearing solids. In *Potassium Argon Dating* (eds. O. A. Schaeffer and J. Zähringer) Springer, pp. 68–106.
- Gabriel U., Gaudet J. P., Spadini L., and Charlet L. (1998) Reactive transport of uranyl in a goethite column; an experimental and modelling study. In *The geochemistry of crustal fluids* (eds. K. V. Ragnarsdottir and E. H. Oelkers), Vol. 151 pp. 107–128. Elsevier.
- Giammer D. (2001) Geochemistry of Uranium at Mineral-Water Interfaces: Rates of Sorption-Desorption and Dissolution-Precipitation Reactions. Ph.D., California Institute of Technology.
- Giral-Kacmarcik S., Savin S. M., Nahon D. B., Girard J.-P., Lucas Y., and Abel L. J. (1998) Oxygen isotope geochemistry of kaolinite in laterite-forming processes, Manaus, Amazonas, Brazil. *Geochim. Cosmochim. Acta* **62** (11), 1865–1879.
- Girard J.-P., Freyssinet P., and Chazot G. (2000) Unraveling climatic changes from intraprofile variation in oxygen and hydrogen isotopic composition of goethite and kaolinite in laterites; an integrated study from Yaou, French Guiana. *Geochim. Cosmochim. Acta* **64** (3), 409–426.
- Girard J.-P., Razanadrano D., and Freyssinet P. (1997) Laser oxygen isotope analysis of weathering goethite from the lateritic profile of Yaou, French Guiana; paleoweathering and paleoclimatic implications. In *Selected papers from the 6th international meeting of EUROLAT on Laterites, palaeoweathering and palaeosurfaces* (eds. Y. Tardy and M. J. Wilson), Vol. 12 pp. 163–174. Pergamon.
- Hautmann S. and Lippolt H. J. (2000) Ar-40/Ar-39 dating of central European K-Mn oxides—a chronological framework of supergene alteration processes during the Neogene. *Chem. Geol.* **170** (1–4), 37–80.
- Hénocque O., Ruffet G., Colin F., and Feraud G. (1998) Ar-40/Ar-39 dating of West African lateritic cryptomelanes. *Geochim. Cosmochim. Acta* **62** (16), 2739–2756.
- Lawrence J. R. and Meaux J. R. (1993) The stable isotopic composition of ancient kaolinites of North America [Monograph] Climate change in continental isotopic records. *Geophys. Mon.* **78**, 249–261.
- Lippolt H. J., Brander T., and Mankopf N. R. (1998) An attempt to determine formation ages of goethites and limonites by (U+Th)- $^4\text{He}$  dating. *Neues Jahr. Mineral.-Monat.* **11**, 505–528.

- Lippolt H. J., Wernicke R. S., and Bähr R. (1995) Paragenetic specularite and adularia (Elba, Italy): Concordant (U + Th)-He and K-Ar ages. *Earth Planet. Sci. Lett.* **132**, 43–51.
- Lovera O., Richter F., and Harrison T. (1989) The  $^{40}\text{Ar}/^{39}\text{Ar}$  thermochronometry for slowly cooled samples having a distribution of diffusion domain sizes. *J. Geophys. Res.* **94**, 17917–17935.
- Lovera O., Richter F., and Harrison T. (1991) Diffusion domains determined by  $^{39}\text{Ar}$  released during step heating. *J. Geophys. Res.* **96**, 2057–2069.
- Osmond J. K. and Cowart J. B. (1992) Ground water. In *Uranium-series disequilibrium; applications to Earth, marine and environmental sciences* (eds. M. Ivanovich and R. S. Harmon), pp. 290–333. Clarendon Press.
- Ozisik M. N. (1989) Boundary Value Problems of Heat Conduction. Dover Publications.
- Reiners P. W. and Farley K. A. (1999) Helium diffusion and (U-Th)/He thermochronometry of titanite. *Geochim. Cosmochim. Acta* **63**, 3845–3859.
- Reiners P. W., Spell T. L., Nicolescu S., and Zanetti K. A. (2004) Zircon (U-Th)/He thermochronometry: He diffusion and comparisons with Ar-40/Ar-39 dating. *Geochim. Cosmochim. Acta* **68** (8), 1857–1887.
- Riebe C. S., Kirchner J. W., and Finkel R. C. (2003) Long-term rates of chemical weathering and physical erosion from cosmogenic nuclides and geochemical mass balance. *Geochim. Cosmochim. Acta* **67** (22), 4411–4427.
- Ruffet G., Innocent C., Michard A., Feraud G., Beauvais A., Nahon D., and Hamelin B. (1996) A geochronological Ar-40/Ar-39 and Rb-87/Sr-87 study of K-Mn oxides from the weathering sequence of Azul, Brazil. *Geochim. Cosmochim. Acta* **60** (12), 2219–2232.
- Savin S. M. and Epstein S. (1970) Oxygen and hydrogen isotope geochemistry of clay minerals. *Geochim. Cosmochim. Acta* **34** (1), 25–42.
- Sharp W. D., Ludwig K. R., Chadwick O. A., Amundson R., and Glaser L. L. (2003) Dating fluvial terraces by Th-230/U on pedogenic carbonate, Wind River Basin, Wyoming. *Quat. Res.* **59** (2), 139–150.
- Shuster D. L. and Farley K. A. (2004)  $^3\text{He}/^4\text{He}$  thermochronometry. *Earth Planet. Sci. Lett.* **217** (1–2), 1–17.
- Shuster D. L., Farley K. A., Sisterson J. M., and Burnett D. S. (2004) Quantifying the diffusion kinetics and spatial distributions of radiogenic  $^4\text{He}$  in minerals containing proton-induced  $^3\text{He}$ . *Earth Planet. Sci. Lett.* **217** (1–2), 19–32.
- Small E. E., Anderson R. S., and Hancock G. S. (1999) Estimates of the rate of regolith production using Be-10 and Al-26 from an alpine hillslope. *Geomorph.* **27** (1–2), 131–150.
- Strutt R. J. (1910) The accumulation of helium in geological time III. *Proc. Royal Soc.* A83, 96–99.
- Tricca A., Porcelli D., and Wasserburg G. M. (2000) Factors controlling the groundwater transport of U, Th, Ra and Rn [Monograph] Isotopic windows on Earth and planetary processes. *Proc. Ind. Acad. Sci.: Earth Planet Sci.* **109** (1), 95–108.
- Tricca A., Wasserburg G. J., Porcelli D., and Baskaran M. (2001) The transport of U- and Th-series nuclides in a sandy unconfined aquifer. *Geochim. Cosmochim. Acta* **65** (8), 1187–1210.
- Vasconcelos P. M. (1998) Geochronology of weathering in the Mount Isa and Charters Towers regions, northern Queensland. CRC LEME Open File Report 68R/E&M Rep. 452R. Perth, Australia, CRC LEME.
- Vasconcelos P. M., Becker T. A., Renne P. R., and Brimhall G. H. (1992) Age and duration of weathering by  $^{40}\text{K}$ - $^{40}\text{Ar}$  and  $^{40}\text{Ar}/^{39}\text{Ar}$  analysis of potassium-manganese oxides. *Science* **258** (5081), 451–455.
- Vasconcelos P. M., Brimhall G. H., Becker T. A., and Renne P. R. (1994a) Ar-40/Ar-39 Analysis of Supergene Jarosite and Alunite—Implications to the Paleoweathering History of the Western USA and West-Africa. *Geochim. Cosmochim. Acta* **58** (1), 401–420.
- Vasconcelos P. M., Renne P. R., Brimhall G. H., and Becker T. A. (1994b) Direct dating of weathering phenomena by  $^{40}\text{Ar}/^{39}\text{Ar}$  and K-Ar analysis of supergene K-Mn oxides. *Geochim. Cosmochim. Acta* **58** (6), 1635–1665.
- Vasconcelos P. M. and Conroy M. (2003) Geochronology of weathering and landscape evolution, Dugald River valley, NW Queensland, Australia. *Geochim. Cosmochim. Acta* **67** (16), 2913–2930.
- Wernicke R. S. and Lippolt H. J. (1993) Botryoidal hematite from the Schwarzwald (Germany): heterogeneous uranium distributions and their bearing on the helium dating method. *Earth Planet. Sci. Lett.* **114**, 287–300.
- Wernicke R. S. and Lippolt H. J. (1994a)  $^4\text{He}$  age discordance and release behavior of a double shell botryoidal hematite from the Schwarzwald, Germany. *Geochim. Cosmochim. Acta* **58** (1), 421–429.
- Wernicke R. S. and Lippolt H. J. (1994b) Dating of vien Specularite using internal (U+Th)/ $^4\text{He}$  isochrons. *Geophys. Res. Lett.* **21** (5), 345–347.
- Wolf R. A., Farley K. A., and Kass D. M. (1998) Modeling of the temperature sensitivity of the apatite (U-Th)/He thermochronometer. *Chem. Geol.* **148**, 105–114.
- Yapp C. J. (1987) Oxygen and hydrogen isotope variations among goethites ( $\alpha$ -FeOOH) and the determination of paleotemperatures. *Geochim. Cosmochim. Acta* **51** (2), 355–364.
- Yapp C. J. (1990) Oxygen isotopes in iron (III) oxides; 1, Mineral-water fractionation factors. *Chem. Geol.* **85** (3–4), 329–335.
- Yapp C. J. (2000) Climatic implications of surface domains in arrays of delta D and delta (super 18) O from hydroxyl minerals; goethite as an example. *Geochim. Cosmochim. Acta* **64** (12), 2009–2025.